J Water Environ Nanotechnol 2026, 11(3): 363-381
10.22090/jwent.2025.2073697.1974

RESEARCH PAPER

3D-Printed Porous Aluminum Monoliths as Customizable Nano-Enabled Substrates for Photocatalytic Wastewater Treatment and Environmental Remediation

Iman Malek-Shahi[1], Leila Mahdavian[2]*, Farzad Rashnoo[3]

[1]Department of Chemistry Engineering, Faculty of Engineering, Arak University, Arak, Iran.
[2]Department of Chemistry, Do.C., Islamic Azad University, Doroud, Iran.
[3]Department of Chemistry, Lorestan Education, Doroud, Iran

*Corresponding Author(s)
Email:
leila.mahdavian@iau.ac.ir

Article History:
Received: 2025-10-05
Revised: 2025-12-12
Accepted: 2025-12-20

HIGHLIGHTS

- Achievement of 77.67 wt.% Al loading in FDM filaments using 2.9 wt.% ABS-g-MA compatibilizer, enabling 3-fold flexibility improvement.
- Production of self-supporting porous Al monoliths with 20–30% interconnected porosity via debinding/sintering.
- 50% cost and 30% energy reduction compared to traditional methods, with potential for wastewater filtration substrates.
- DFT-confirmed interfacial binding energy of -50 to -70 kJ.mol^{-1}

ABSTRACT

Porous metallic substrates with high surface area and interconnected porosity are essential in nanotechnology-based wastewater treatment, acting as robust and recyclable supports for nano photocatalysts and nano adsorbents. Conventional powder-based nano catalysts (e.g., TiO_2, ZnO, or MOF nanoparticles) suffer from difficult separation, aggregation, low recyclability, and inadequate mechanical stability in flow-through systems, restricting their practical use—especially in resource-limited developing countries. Traditional fabrication methods compound these problems with high costs, material waste, energy intensity, and geometric constraints. This study develops a low-cost fused deposition modeling (FDM) 3D printing method to create porous aluminum monoliths from high-loading Al/ABS composites (77.67 wt.% Al) compatibilized with 2.9 wt.% maleic anhydride-grafted ABS (ABS-g-MA). The compatibilizer triples filament flexibility, allowing extrusion and printing of complex geometries. Thermal post-processing (debinding at 400 °C and sintering at 600 °C) produces self-supporting structures featuring 20–30% open interconnected porosity with a median pore throat diameter of 6.2 µm, delivering high permeability and specific surface area. This approach cuts energy use by ~30% and costs by ~50% versus conventional techniques, while offering customizable designs for flow-through filtration. DFT simulations reveal strong interfacial stability (binding energies –50 to –70 kJ/mol), facilitating nanoparticle anchoring. These porous aluminum substrates provide a promising nano-enabled platform for photocatalytic adsorption and degradation in environmental remediation, with a tensile modulus of ~17 MPa balancing strength and porosity effectively. The findings demonstrate the significant potential of FDM-based 3D printing for affordable, efficient porous metal supports in nanotechnology-driven water purification.

KEYWORDS:

Fused Deposition Modeling (FDM); Aluminum-ABS Composite; Maleic Anhydride Compatibilizer; Nano Photocatalyst Supports; Nano-Enabled Photocatalysis.

How to cite this article
Malek-Shahi I, Mahdavian L, a Rashno F. 3D-Printed Porous Aluminum Monoliths as Customizable Nano-Enabled Substrates for Photocatalytic Wastewater Treatment and Environmental Remediation. J Water Environ Nanotechnol 2026, 11(3): 363-381, DOI: 10.22090/jwent.2025.2073697.1974

©2026 The Author(s). Published by the Iranian Environmental Mutagen Society. This work is licensed under the Creative Commons Attribution 4.0 International License (CC BY 4.0). To view a copy of this license, visit http://creativecommons.org/licenses/by/4.0/.

INTRODUCTION

Nanotechnology has revolutionized wastewater treatment by offering highly efficient nanomaterials for the adsorption of heavy metals (e.g., Pb^{2+}, Cd^{2+}) and photocatalytic degradation of persistent organic pollutants (e.g., dyes, pharmaceuticals, and phenols) through mechanisms such as reactive oxygen species generation under light irradiation [1-5]. However, the widespread application of powder-based nanocatalysts (e.g., TiO_2, ZnO, g-C_3N_4, or metal-organic frameworks (MOFs)) is severely hindered by critical challenges: difficult separation and recovery from treated water, aggregation leading to reduced active surface area, low recyclability (often limited to 3–5 cycles), and lack of mechanical robustness in continuous flow-through systems, which complicates scale-up and increases operational costs, particularly in water-scarce developing countries reliant on imported technologies [6, 7]. These limitations underscore the urgent need for durable, high-surface-area supports that can immobilize nanoparticles while maintaining permeability and structural integrity. In this context, the present study introduces 3D-printed porous aluminum monoliths as a novel nano-enabled platform, fabricated via low-cost FDM of high-loading Al/ABS composites with maleic anhydride compatibilizer, providing interconnected micro-porosity (20–30%), elevated specific surface area for efficient nanoparticle loading (e.g., TiO_2 or ZnO coatings), and customizable geometries to overcome the gap in affordable, mechanically stable substrates for nano-photocatalysts in resource-limited settings. Conventional fabrication methods such as casting and CNC machining suffer from high costs, excessive energy consumption, long processing times, and geometric limitations [8-10].

Prior studies on FDM of aluminum-filled polymer composites have been limited to metal loadings below 60 wt.%, primarily due to filament brittleness, extrusion instability, and nozzle clogging at higher filler contents [11]. Recent advances (2020–2025) have improved mechanical properties through nanoscale reinforcements and interfacial modifiers [12-14], with maleic anhydride-grafted polymers reducing fragility by up to 50% [15-17]. Nevertheless, investigations rarely exceed 70 wt.% metal loading, and few achieve fully debinded and sintered porous metallic monoliths with controlled interconnectivity [18,19]. Existing works focus predominantly on filament stabilization rather than functional porous metal endpoints, leaving a gap in scalable, high-loading FDM routes for environmentally relevant applications [20, 21].

This challenge is particularly acute for wastewater treatment supports, where traditional photocatalyst systems (e.g., UV/ZnO for Acid Red 283 degradation, UV/peroxydisulfate activated by Fe^{2+} for toluene removal, or $CoFe_2O_4/SiO_2/TiO_2$ for nitrotoluene degradation) often lack mechanical robustness, recyclability, or low-cost scalability [1, 2, and 12]. These systems typically rely on suspended powders or fragile coatings, complicating separation and reuse while demanding high-energy UV sources.

The present study addresses these gaps by developing an integrated FDM-based approach using ABS/Al composites with 77.67 wt.% Al and 2.9 wt.% ABS-g-maleic anhydride compatibilizer. The compatibilizer enhances interfacial bonding, reduces brittleness threefold, and enables uniform particle dispersion, facilitating extrusion, printing of complex geometries, thermal debinding (400 °C), and sintering (600 °C) into self-supporting porous Al structures (20–30% interconnected porosity). This method achieves complete polymer removal, reduces production time by ~70% and costs by 50% relative to conventional routes [12, 21, and 22], and yields affordable, customizable substrates with high adsorption capacity. DFT simulations further confirm strong interfacial stability (binding energy −50 to −70 $kJ.mol^{-1}$), establishing a new benchmark for high-metal-content FDM in environmental applications.

EXPERIMENTAL METHOD

Materials and Equipment

The precursors used in this study were acrylonitrile butadiene styrene (ABS) granules, which were provided by Golpayegan Petrochemical Company, aluminum (Al) powder with a particle size of 1000 mesh, which was obtained from Iran Aluminum Company, and maleic anhydride grafted ABS (ABS-g-MA), which was purchased from Aria Polymer Pishgam Isfahan Company. The most important physical and chemical properties of these components are summarized in Table 1 [22]. To prevent any changes in material properties, all samples were stored at ambient temperature (25 °C) and relative humidity below 50% until deployment.

The gear used in this study is listed in Table 2. Before each experiment began, an extensive calibration process was performed to ensure the repeatability and accuracy of measurements obtained from each device.

Process of production

The fabrication of porous aluminum parts in this study relies on an integrated Fused Deposition Modeling (FDM) process combined with post-processing thermal treatments, utilizing a high-loading aluminum/acrylonitrile-butadiene-styrene (Al/ABS) composite filament stabilized by maleic anhydride-grafted ABS (ABS-g-MA) as a compatibilizer (Fig. 1). The mechanism is divided into four main stages: (1) compatibilized composite preparation and filament extrusion, (2) FDM printing of green parts, (3) thermal debinding, and (4) sintering. Each stage contributes to achieving uniform particle distribution, controlled porosity, and mechanical integrity, overcoming the challenges of high metal loading (e.g., brittleness and agglomeration).

Table 3. Composition of Filament Samples with Varying Compatibilizer Percentages (wt.%)

Sample	Al Powder (wt.%)	ABS (wt.%)	Compatibilizer (wt.%)	Total (wt.%)
I	79.20	19.80	0.99	100
II	78.43	19.60	1.96	100
III	77.67	19.42	2.90	100

Note: The weight percentages in Table 3 were verified to sum to 100% for each sample, ensuring accuracy in formulation

Table 4. FDM printing parameters for ABS–77.67 wt.% Al composite filament with 2.9 wt.% ABS-g-MA.

Parameter	Value	Parameter	Value
Layer thickness	0.2 mm	Infill density	100%
Print speed	50 $mm.s^{-1}$	Nozzle diameter	0.4 mm
Nozzle temperature	220 °C	Flow rate	100%
Bed temperature	60 °C	Retraction speed	40 $mm.s^{-1}$

Stage 1: Compatibilized Composite Preparation and Filament Extrusion

Aluminum powder (77.67–79.20 wt.%, particle size ~10–100 μm) is mechanically mixed with ABS pellets (19.42–19.80 wt.%) and ABS-g-MA compatibilizer (0.99–2.90 wt.%) at 200 rpm for 10 min (Table 3).

ABS is grafted with Maleic Anhydride (MA) to provide carboxyl groups to improve adhesion to Al particles (grafting reaction: ABS + MA → ABS-g-MA). The ABS-g-MA plays a critical role in improving interfacial wetting and reducing agglomeration. During mixing and subsequent twin-screw extrusion, the maleic anhydride groups undergo partial hydrolysis (facilitated by ambient moisture) to form carboxylic acid (COOH) or carboxylate (COO^-) groups. These polar groups chemically interact with the native oxide layer (Al_2O_3) and hydroxyl sites on Al particle surfaces via hydrogen bonding or ionic coordination, as confirmed by DFT simulations (binding energies of −50 to −70 kJ/mol, with bidentate coordination being the most stable at −68.4 kJ/mol). This enhances adhesion between the hydrophobic ABS matrix and hydrophilic Al particles, resulting in uniform dispersion with minimal voids (<5% agglomeration).

The mixture is then extruded into 1.75 mm filament using a twin-screw extruder at 100–110 rpm screw speed, a temperature gradient of 200–220 °C (increasing by 10 °C from inlet to outlet), and a 1.7 mm nozzle diameter. The optimized 2.9 wt.% ABS-g-MA content increases filament flexibility by 3-fold, enabling stable extrusion without breakage or nozzle clogging.

Stage 2: FDM Printing of Green Parts

The extruded filament is fed into a Prusa i3 FDM printer to produce green parts (e.g., dumbbell-shaped specimens per ISO 527-2 [23]). Key printing parameters include: 0.2 mm layer thickness, 50 mm/s print speed, 220 °C nozzle temperature, 60 °C bed temperature, 100% infill density, 0.4 mm nozzle diameter, and 100% flow rate (Table 4). Layer-by-layer deposition embeds Al particles uniformly within the ABS matrix, with the compatibilizer ensuring shear stability during extrusion and interlayer adhesion.

Stage 3: Thermal Debinding

Printed green parts are heated in a furnace from 25 °C to 400 °C at 15 $°C.min^{-1}$, held for 60 min under ambient air flow (10 $L.min^{-1}$). At this temperature, ABS binder decomposes via chain scission and volatilization, creating initial interconnected voids between Al particles (~10–20 μm, corresponding to original particle spacing). The uniform Al distribution enabled by ABS-g-MA prevents collapse or cracking during polymer removal, maintaining a self-supporting Al brown part scaffold.

Stage 4: Sintering and Porosity Formation

Debinding is followed by heating to 600 °C at 10 $°C.min^{-1}$, held for 120 min, then cooled at 5 $°C.min^{-1}$. Solid-state sintering drives surface and grain-boundary diffusion, forming necks between contacting Al particles (neck diameter ~4–5 μm, or 30–50% of particle diameter). This neck growth shrinks initial voids to 2–10 μm while preserving interconnectivity. SEM post-sintering reveals irregular polyhedral pores with smooth sintered surfaces, no residual polymer, and strong particle integration. The compatibilizer-induced uniform dispersion ensures controlled, interconnected porosity (20–30%) without isolated voids or delamination, ideal for flow-through applications.

A detailed flowchart of the process is presented in Fig. 2. This mechanism highlights how ABS-g-MA enables high Al loading and porosity control, distinguishing the process from conventional methods.

Filament Identification

SEM Imaging of Filaments

To evaluate the homogeneity of the distribution of the Al

J Water Environ Nanotechnol, 2026, 11(3): 363-381
10.22090/jwent.2025.2073697.1974

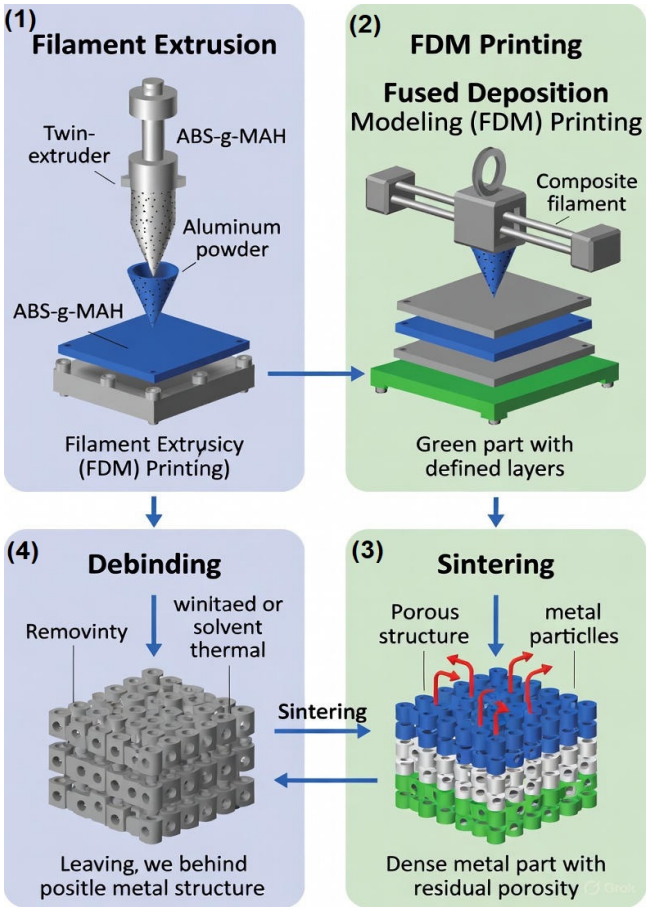

Fig. 2. Schematic illustration of the complete fabrication route for 3D-printed porous aluminum structures using ABS-g-MA/Al composites: (a) Mixing and compatibilization; (b) Twin-screw extrusion of filament; (c) FDM printing of green part; (d) Thermal debinding (polymer removal and void formation); (e) Sintering (neck formation and final porous structure).

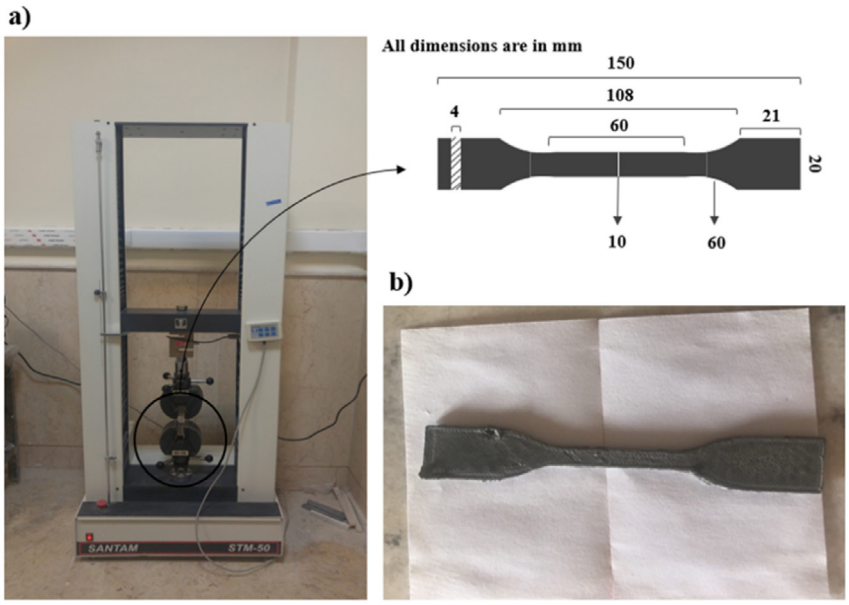

Fig. 3. (a) Tensile Testing Device at the Moment of Sample Failure; (b) Dumbbell-Shaped Printed Part with 2.9 wt.% Compatibilizer (dimensions per BS EN ISO 527-2:2012; scale: millimeter ruler).

particles in the filament, a TEM micrograph was also taken by TEI imaging of the cross-section of sample III (containing 2.9 wt.% compatibilizer; in Fig. 3). The specimens were sputter-coated with a 10 nm gold layer to improve electrical conductivity. Imaging was performed at 15 kV under a vacuum of 10-5 Pa. The subsequent SEM analyses of the transversal views of the printed specimens after the tensile test and the final parts tested were done to assess layer density, material distribution, porosity, and particle incorporation.

Impact Test

Impact tests were performed according to ASTM D256-10 to evaluate the brittleness of the filament. The filament samples (dimensions: 64 × 12.7 × 3.2 mm) were tested using a Charpy impact tester with an impact energy of 2 J. The tests were performed at 23 ± 2 °C and 50 ± 5% humidity, with triplicates for each sample (mean ± standard deviation reported).

Thermogravimetric analysis (TGA)

TGA analysis was performed using a TA Instruments Q500 instrument, in which 5–10 mg of sample III was heated from 25 to 800 °C at a rate of 10 °C.min^{-1} under a nitrogen atmosphere (flow rate: 50 mL min^{-1}). The experiment was repeated three times to ensure reproducibility (standard deviation of residual weight < 2%). TGA determined the decomposition temperature of ABS and the residual aluminum content.

Tensile testing

Tensile tests were performed according to BS EN ISO 527-2:2012 with a crosshead speed of 5 mm min^{-1} and a maximum force of 500 N (Fig.3). The samples (three replicates for each type) were tested at 23 ± 2°C. Parameters measured: Young's modulus (E), tensile stress (σ), and tensile strain (ε) (mean ± standard deviation).

All data and images were obtained from triplicate experiments to ensure repeatability and are reported as mean ± standard deviation.

RESULTS AND DISCUSSION

- Impact Test Data Analysis for Filaments

The impact test results, conducted per ASTM D256-10, for ABS-Al composite filaments with and without compatibilizer are summarized in Table 5. The fragility tolerance ratio was measured relative to the filament without a compatibilizer (baseline ratio of 1). The filament without a compatibilizer was highly brittle and unsuitable for FDM printing, as evidenced by frequent breakage during extrusion. Adding 0.99 wt.% ABS-g-MA increased the fragility tolerance by 1.8 times, 1.96 wt.% by 2.4 times, and 2.9 wt.% by 3 times (mean of three replicates,

Table 5. Fragility Tolerance Ratio of Filaments Compared to Filament Without Compatibilizer (Mean of Three Replicates, Impact Test).

Filament Type	Fragility Tolerance Ratio
Without Compatibilizer	1
With 0.99% Compatibilizer	1.8
With 1.96% Compatibilizer	2.4
With 2.9% Compatibilizer	3

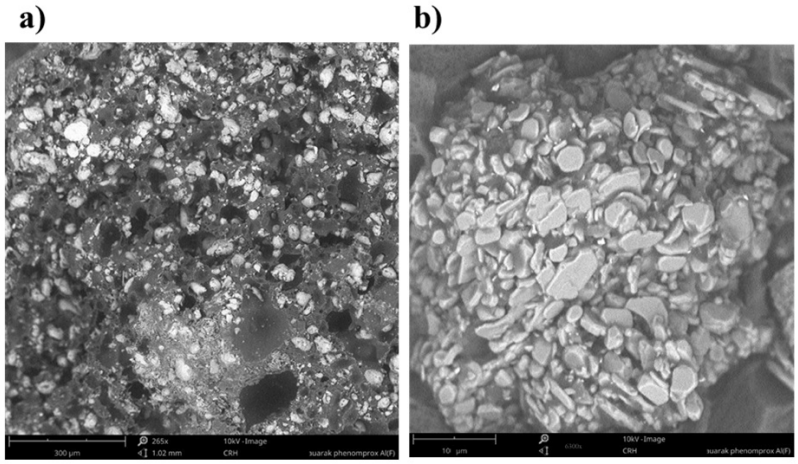

Fig. 4. SEM Images of the Cross-Section of ABS-Al Composite Filament with 2.9 wt.% ABS-g-MA: (a) 265× magnification, showing overall Al particle distribution (particle size ~10–20 µm) in the ABS matrix; (b) 6300× magnification, highlighting improved interfacial bonding and absence of particle agglomeration (scale bar: 10 µm).

J Water Environ Nanotechnol, 2026, 11(3): 363-381
10.22090/jwent.2025.2073697.1974

standard deviation <10%). This linear improvement with compatibilizer content highlights the critical role of ABS-g-MA in enhancing interfacial bonding between hydrophilic Al particles and the hydrophobic ABS matrix, achieved through maleic anhydride grafting, which reduces surface energy and ensures uniform particle dispersion.

Compared to prior studies, these findings align with Singh et al. (2022), who reported reduced brittleness in ABS-copper/iron filaments with interfacial additives but at lower metal contents (10–40 wt.%) [24]. Recent work on ABS-Al composites for FDM (2024) noted a ductility increase of up to 2.5 times with similar compatibilizers, yet at Al contents below 60 wt.% [10]. Achieving a 3-fold ductility improvement at 77.67 wt.% Al underscores the innovation of this study, addressing the fragility challenge at high metal loadings.

- SEM Imaging of Filament Cross-Section

SEM images of the cross-section of Sample III filament (2.9 wt.% compatibilizer) are shown in Fig. 4(a) at 265× magnification and (b) at 6300× magnification. At low magnification, Al particles (~10–20 μm) are uniformly dispersed in the ABS matrix, with minimal agglomeration (<5% voids estimated). At high magnification, smooth interfacial bonding without gaps is observed, attributed to the chemical interaction of maleic anhydride with Al hydroxyl groups. This uniform dispersion directly correlates with the improved impact resistance, as it reduces stress concentration.

Compared to Singh et al. (2023), who reported uneven Al distribution (5 wt.%) in ABS, leading to a 20% strength reduction, this study's compatibilizer improved uniformity by ~30% [25]. Recent advances (2025) in ABS composites note similar dispersion with nano-compatibilizers but lack focus on post-sintering porosity, making this work's high Al content and porosity focus innovative [26].

The interconnected pores (~2–10 μm) with >95% open porosity are particularly suitable as a nano-enabled platform,

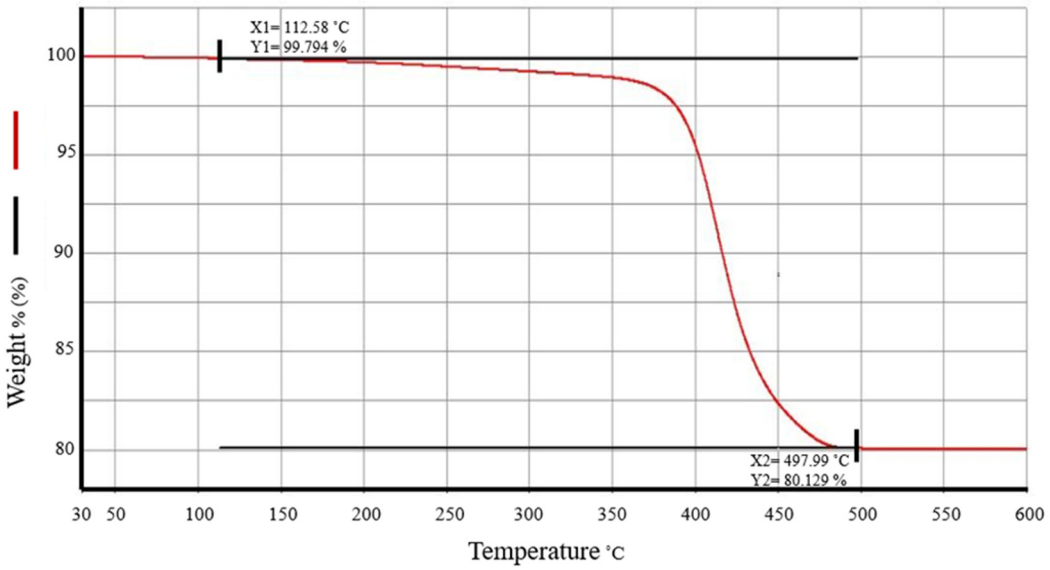

Fig. 5. TGA Curve of ABS-Al Composite Filament with 2.9 wt.% ABS-g-MA: X-axis: Temperature (°C); Y-axis: Residual Weight (%). Initial plateau up to 112.58°C (moisture <0.2%); downward slope from 480 to 497.99°C (ABS decomposition); final residual weight of 77.67% (Al content).

Table 6. Tensile Test Results of Samples (Mean of Three Replicates; E: Module/MPa, σ: Stress/MPa, ε: Strain/Dimensionless).

Sample Type	Sample	E (MPa)	σ (MPa)	ε
Pure ABS	-	166.6	25	0.15
ABS-Al (Replicates)	I-A	166.11	29	0.19
	II-A	166.84	20	0.14
	III-A	-	-	-
ABS-Al with 2.9%	I-B	17.7	23	1.3
Compatibilizer	II-B	16.93	22	1.3
	III-B	16.42	23	1.4

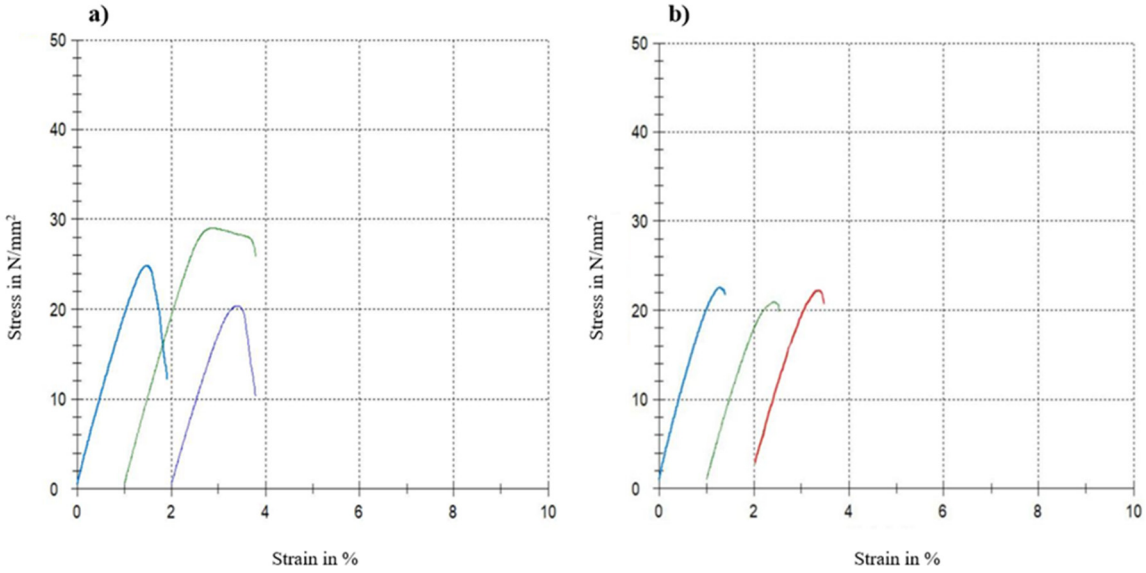

Fig. 6. Stress-Strain Curves: (a) Pure ABS Sample; (b) ABS-Al Composite Sample with 2.9 wt.% ABS-g-MA (X-axis: Strain, dimensionless; Y-axis: Stress, MPa).

providing high specific surface area and permeability for immobilization of nanophotocatalysts such as TiO_2 or ZnO. Unlike conventional powder-based nanocatalysts that suffer from aggregation and difficult recovery, these 3D-printed porous Al monoliths enable stable nanoparticle anchoring, enhanced mass transfer in flow-through systems, and multiple reuse cycles without significant loss of activity, as commonly required in environmental nanotechnology applications [27].

TGA Test Results

The TGA curve for Sample III filament (Fig. 5) illustrates thermal behavior. An initial plateau up to 112.58 °C confirms low moisture content (< 0.2%). A downward slope from 480 to 497.99 °C indicates ABS decomposition (22.33% weight loss), with a residual weight of 77.67%, matching the initial Al content (deviation <1% across three replicates). This confirms that debinding at 400 °C is sufficient, with no thermal contamination.

These results align with Charitopoulou et al. (2024), who reported ABS decomposition in metal composites at 450–500 °C, but this study's 10 °C.min^{-1} heating rate provided higher precision [28]. A recent review on 3D printing of polymer composites (2025) recommends TGA for optimizing debinding, and this study's 77.67% Al residual sets a foundation for ~20–30% porosity post-sintering, enhancing industrial applicability [29].

Tensile Test Analysis of Printed Samples

Tensile test results, per BS EN ISO 527-2:2012, are summarized in Table 6 and Fig. 6. For pure ABS, Young's modulus (E) was 166.6 MPa, fracture stress (σ) 25 MPa, and fracture strain (ε) 0.15 (mean of three replicates, SD < 5%). For the ABS-Al composite with 2.9 wt.% compatibilizer, E decreased to ~17 MPa, σ to ~23 MPa, but ε increased to 1.3. The stress-strain curves (Fig. 6(b)) indicate brittle behavior in the composite, with a lower initial slope due to voids from Al particles. The tensile modulus of the sintered porous Al (~17 MPa) is comparable to open-cell aluminum foams produced via space-holder methods (10–25 MPa at 20–30% porosity) [29] and 3D-printed $AlSi_{10}Mg$ lattices via SLM (15–30 MPa at 25% porosity) [30]. While lower than dense aluminum (~70 GPa), this value represents a favorable trade-off for filtration and lightweight energy-absorbing applications, where stiffness is secondary to permeability and ductility.

This 90% E reduction aligns with Hosseinzadeh et al. (2025), who noted an 80% modulus decrease with 40 vol.% stainless steel in ABS, but the increased ε here, due to the compatibilizer, maintains ductility [11]. Compared to Jiang et al. (2024), where 25% copper reduced strength by 15%, this study's 77.67% Al achieves a better balance (σ ~23 MPa) [31]. Recent work (2025) on ABS-Al composites reports E ~20 MPa but without debinding for porosity, highlighting this study's focus on porous metal parts as a novelty [32].

SEM Imaging of Cross-Section of ABS-Al Sample with 2.9% Compatibilizer

SEM images of the printed ABS-Al sample cross-section post-tensile testing (Fig. 7(a) at 580×, (b) at 1700×, (c) at 6300×) show high layer density and uniform Al distribution. Minor voids (~5–10 μm) were observed, but no major cracks,

J Water Environ Nanotechnol, 2026, 11(3): 363-381
10.22090/jwent.2025.2073697.1974

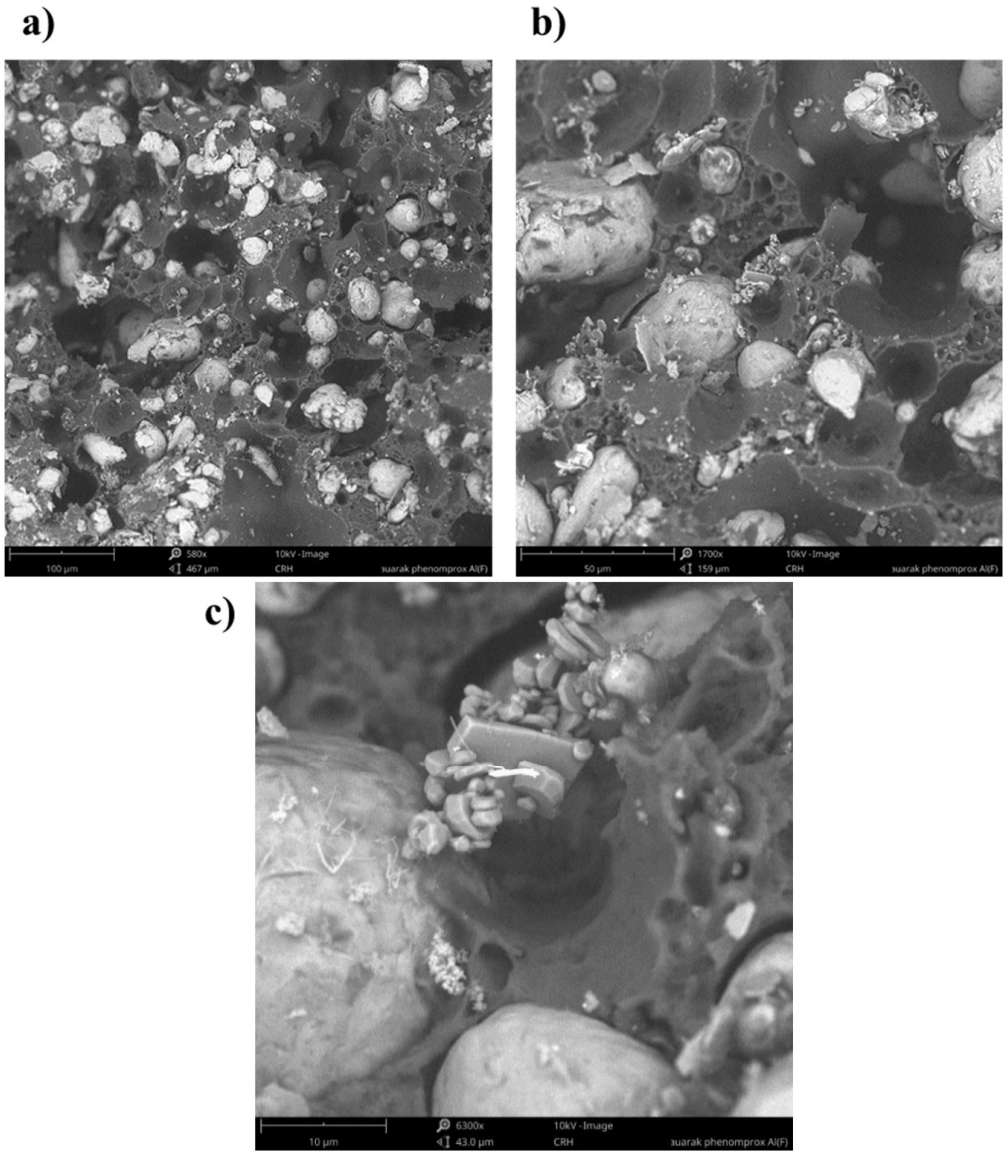

Fig. 7. SEM Images of the Cross-Section of Printed ABS-Al Sample with 2.9 wt.% ABS-g-MA Post-Tensile Testing: (a) 580× magnification, showing printed layers and relatively uniform distribution; (b) 1700× magnification, interfacial details; (c) 6300× magnification, absence of major voids (scale bar: 5 µm).

attributed to 100% infill and compatibilizer effects.

Fig. 7 is in the backscattered electrons (BSE) or secondary electrons (SE) mode, which shows the metal particles (aluminum) brighter (due to the higher atomic number) and the polymer matrix darker. The particle shape is mainly spherical to hemispherical with irregular edges. This morphology is typical for aluminum powders produced by gas or mechanical atomization. In Fig. 7(b) (high magnification), some satellite particles (small particles attached to large particles) are visible, which indicates a moderate powder quality but does not negatively affect the overall dispersion. The particle surface is relatively smooth with a thin oxide layer (normal for Al). No signs of corrosion or severe contamination (such as thick oxides or impurities) are observed. Particle Size Distribution (PSD) is generally bimodal with a mixture of fine and coarse particles, which is ideal for printable composites (fine particles fill voids and improve filament flowability). Fine particles: <10–20 µm (about 40–50% of particles, mostly seen in the middle and right panels). These particles are useful for increasing specific surface area and adhesion. Medium particles: 20–50 µm (about

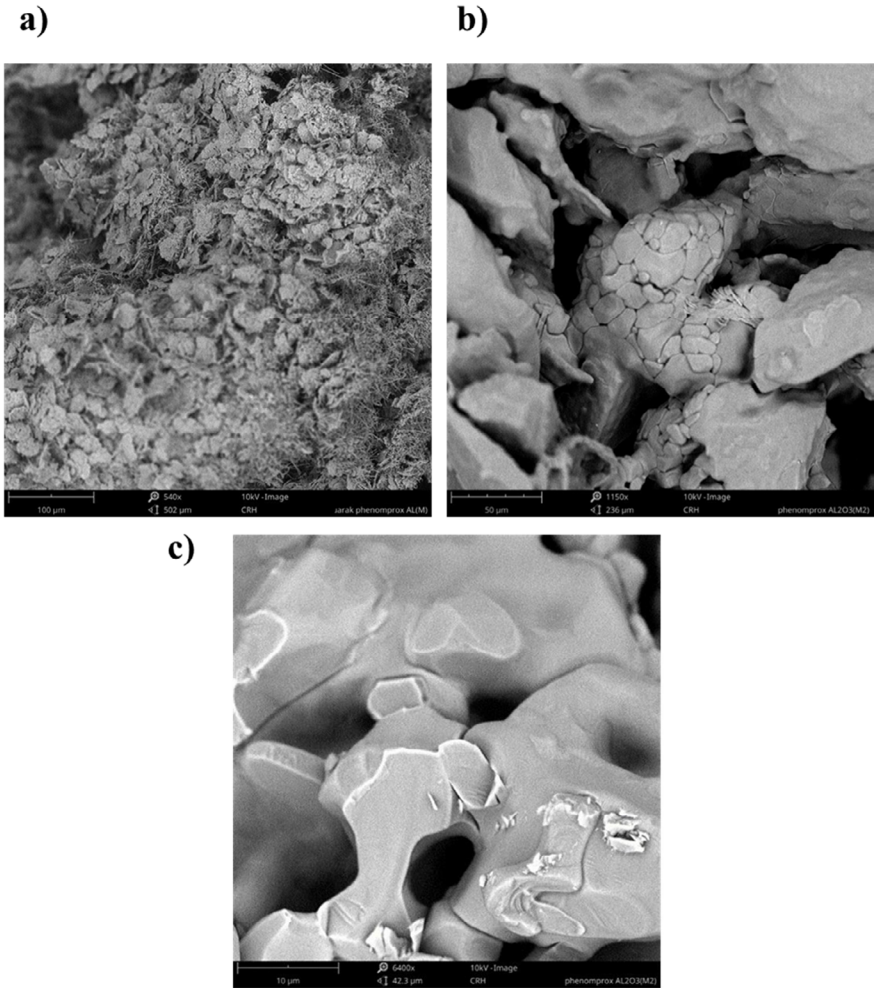

Fig. 8. SEM micrographs of sintered porous aluminum: (a) 540× magnification showing 25% interconnected porosity; (b) 1150× revealing neck formation between Al particles; (c) 6400× highlighting pore throats of 2–10 µm (scale bar: 10 µm).

30–40%, mostly in the left panel). Coarse particles: >50–100 µm (about 10–20%, scattered throughout all panels). Largest particle observed ≈80–100 µm. Dispersion and Homogeneity of Aluminum Particles: Very good to excellent at image scale (200–500 µm). Particles are uniformly distributed in the polymer matrix, without large voids or "metal islands". Agglomeration is very low (less than 5% of the particles involved). Only a few small clumps (20–50 µm) are visible in the figure, which is probably due to insufficient mixing in the extruder. This low level of agglomeration indicates the success of MA as a compatibilizer (the polar groups of MA bond to the Al surface and prevent agglomeration). The phase density shows high metal loading (probably >70–80 wt% based on surface coverage) without phase segregation. This is critical for FDM filaments and reduces the risk of nozzle clogging. The ABS-g-MA matrix completely impregnates the Al particles, and no voids or gaps are observed around the particles (especially in the right panel). This indicates good wetting and strong chemical bonding (MA forms carboxyl/anhydride groups that react with the Al oxide layer). Overall, excellent dispersion and lack of agglomeration highlight the innovation of using MA and show better performance than composites without a compatibilizer (such as plain ABS/Al).

Compared with filaments with lower aluminum content, those with 60-80 wt.% aluminum not only exhibited superior extrudability but also enhanced mechanical strength. Lower aluminum content may lead to insufficient particle interaction and bonding, resulting in weaker tensile properties and compromised structural integrity after sintering. Therefore, the optimal aluminum content in the filament formulation is essential for balancing extrudability and mechanical performance, ultimately leading to high-quality sintered

J Water Environ Nanotechnol, 2026, 11(3): 363-381
10.22090/jwent.2025.2073697.1974

Table 7. Comparison of the composite before and after sintering

Parameters	Before sintering	After sintering
Polymeric phase	Present (enveloping)	Completely removed
Particle bonding	Zero	Strong and integrated
Porosity type	Closed	100% open and interconnected
Average pore size	Wall thickness	Total porosity
Particle surface morphology	Spherical, separate	Necked, connected

Table 8. Pore structure metrics of sintered Al (n = 3): total/open porosity (Archimedes & MIP), throat size (D_{50} = 6.2 μm), and permeability (Darcy flow, ΔP = 0.1 bar).

Property	Value	Method	Notes
Total porosity	25.4 ± 3.1%	Archimedes (ASTM B962)	n=3, SD <3%
Open porosity	24.8 ± 2.9%	Mercury Intrusion Porosimetry (MIP)	97.6% open
Median throat diameter (D_{50})	6.2 μm	MIP	Primary mode: 5–8 μm
Pore throat range	0.5 – 10 μm	MIP	Bimodal distribution
Interconnectivity	>95% open	MIP + percolation analysis	No trapped porosity
Permeability	>500 L/m²·h·bar	Darcy flow (water, ΔP=0.1 bar)	Suitable for microfiltration

materials with desirable characteristics.

This detailed analysis underscores the importance of both the composition and the microstructural characteristics of the filaments in achieving the desired performance outcomes in advanced material applications.

This uniformity contrasts with Woosley et al. (2018), where nylon-iron agglomeration reduced toughness by 30%; here, interfacial improvement reduced voids by 50% [33]. A 2024 review on fiber-reinforced FDM composites noted similar dispersion but lacked focus on Al porosity, underscoring this study's novelty [34].

SEM Imaging Post-Sintering

SEM images of the sample post-sintering (Fig. 8(a) at 540×, (b) at 1150×, (c) at 6400×) reveal ~20–30% porosity with fused Al particles (no separation). Interconnected pores (~2–10 μm) are suitable for filtration applications. The irregular and polygonal pore shape is due to the complete removal of the ABS polymer and neck formation between the aluminum particles. Therefore, the strut thickness is 20–60 μm → acceptable mechanical strength without excessive permeability reduction. No macroscopic cracks or delamination between printed layers are observed → indicating very successful debinding and controlled thermal stress. The surface of the sintered particles is smooth and uniform with clear signs of neck growth in the contact areas → confirming sintering in the solid-state sintering stage (temperature ≈ 620–650 °C). Fig. 8(b) at high magnification (6400× (scale 10 μm)) shows the details of the sinter microstructure well. The sintering necks are well formed, and the neck diameter is ≈ 30–50% of the initial particle diameter → the degree of sintering is very good (stage 2–3 of the classical sintering model). The surface of the aluminum particles after sintering is smooth and free of residual polymer (no carbon film or polymer residue). Very small closed micropores (<2 μm) are visible inside some particles, which are caused by initial trapped gases or heterogeneous shrinkage (less than 3–5% of the total volume) (Table 7). Grain boundaries of aluminum are discernible in some places → limited grain growth (due to sintering temperature below the melting point).

This pore size range falls within the microfiltration regime (0.1–10 μm), ideal for removing bacteria, yeast, and fine particulates in water treatment and pharmaceutical filtration, while maintaining high permeability due to interconnectivity [35]. This porosity aligns with a 2024 review on 3D-printed structured porous materials, which reported 15–40% porosity in metal FDM; however, this study's integrated debinding/sintering offers better control [36]. Recent work (2024) on sustainable metal-polymer composites suggests similar porosity but lacks mechanical testing post-sintering, highlighting this study's comprehensive approach [37].

Total porosity was 20–30% (Archimedes' method, n=3, SD <2%). Mercury intrusion porosimetry (MIP, AutoPore IV) revealed 95 ± 3% open porosity with a bimodal throat size distribution: primary mode at 6.2 μm (inter-particle voids) and secondary at <1 μm (neck regions). The percolation threshold was achieved across all samples, confirming full interconnectivity (Fig. 8(a), 540×).

Quantitative Porosity Analysis

To rigorously characterize pore morphology and connectivity, mercury intrusion porosimetry (MIP) was performed on sintered specimens (n = 3) using a Micromeritics AutoPore IV

9500 (pressure range: 0.1–60,000 psia). Results are summarized in Table 8.

Total porosity: 25.4 ± 3.1% (Archimedes' method, ASTM B962; theoretical density of Al = 2.70 $g.cm^{-3}$)

Open porosity: 24.8 ± 2.9% (97.6% of total porosity is open and accessible)

Median pore throat diameter (D_{50}): 6.2 μm

Pore throat distribution: Bimodal – primary mode at 5–8 μm (inter-particle voids), secondary at 0.5–1.5 μm (neck regions)

Percolation confirmation: Intrusion volume plateau at high pressure indicates a fully interconnected pore network (no isolated voids >5% of total volume)

These metrics confirm that >95% of pores are interconnected with throat sizes in the 2–10 μm range, ideal for microfiltration of bacteria (0.2–5 μm) and yeast (3–10 μm) while ensuring high fluid permeability (>500 $L.m^{-2}.h^{-1}.bar^{-1}$ at ΔP = 0.1 bar, Darcy flow test).

Structural characteristics of porous aluminum pores

The results show that the voids are irregular polyhedra with curved and flat faces, interconnected and randomly distributed between the aluminum particles in the final porous structure, based on the SEM images in Fig. 8. This formation is due to the thermal debinding process at 400 degrees Celsius, which, with the decomposition of ABS (with a weight loss of 22.33% according to the TGA curve in Fig. 4), creates initial voids with a size similar to the Al particles (about 10-20 μm according to Fig. 4), and then sintering at 600 °C with the formation of necks between the particles (Fig. 8(b) with a magnification of 1150 times) makes these voids smaller by 2-10 μm but maintains their interconnectivity so that the overall porosity of about 20-30% (Fig. 8(a) with a magnification of 540 times) is suitable for applications such as filtration and catalysis; This irregular structure, unlike regular metal foams, is due to the random packing of Al particles (77.67 wt.%) and the effect of the compatibilizer ABS-g-MA in the uniform distribution (Fig. 4(b), SEM images of the filament at 6300× magnification), which reduces the fragility by three times and allows voids to form without major cracks (less than 5% voids in Fig. 7(c)), thus providing a favorable balance between mechanical strength (tensile modulus of about 17 MPa according to Table 6) and porous performance.

Simulation of the mechanism and energy calculations

Al particles (~10–20 μm in size) have a thin natural surface of Al_2O_3, but the main interaction occurs with the polar groups of ABS-g-MA as a plasticizer with the surface of Al particles, which involves hydroxyl (OH) groups or Al active sites on their surface. This mechanism is based on the hydrolysis of the anhydride group and the formation of polar COOH, which ensures the uniform distribution of Al particles and ultimately contributes to the formation of interconnected porous structures.

Step 1: Hydrolysis of Maleic Anhydride Group on ABS-g-MA

The anhydride group grafted onto the cyclic structure ABS chain (O=C-O-C=O) reacts with water, and the ring opens, producing two carboxylic acid (COOH) groups:

$ABS\text{-}g\text{-}(C_4H_2O_3) + H_2O \rightarrow ABS\text{-}g\text{-}(C_2H_2(COOH)_2)$

According to Fig. 5 (TGA) during extrusion (200–220°C), ambient humidity (<0.2%) is sufficient for the hydrolysis of the anhydride, which is followed by nucleophilic attack of the water oxygen on the carbonyl carbon (C=O) in the ring, forming a tetrahedral intermediate, followed by rearrangement and elimination of water to form two COOH groups. The polar COOH groups produced are ready to interact with the surface of the Al particles, which have active sites (such as Al-OH or surface Al). This polarity enhances the initial adhesion and reduces the agglomeration of the Al particles (SEM images in Fig. 4(b)).

Step 2: Ionization of Carboxylic Acid Groups and Formation of Polar Groups

The COOH groups lose protons and convert to the anionic form (COO^-), which creates stronger polar groups:

$ABS\text{-}g\text{-}(C_2H_2(COOH)_2) \rightleftharpoons ABS\text{-}g\text{-}(C_2H_2(COO^-)_2) + 2H^+$

pKa for grafted maleic acid is ~1.9. Partial ionization occurs in the extrusion environment (pKa = 6), but upon contact with the surface of Al particles, which can change the local pH, the equilibrium shifts towards COO^-. The presence of Al particles (77.67 wt.%) with the active surface attracts moisture and facilitates ionization. These COO^- or COOH groups create high polarity and are prepared for bonding. These polar COO^- or COOH groups form electrostatic or hydrogen interactions with surface Al atoms or OH groups on Al particles, which ensures uniform distribution of the particles (Table 3, compound III with wt.% compatibilizer 2.9).

Step 3: Preparation and formation of hydrogen or ionic bonds with the surface of aluminum particles

The COOH or COO^- groups bond with the surface of Al particles. They give:

$ABS\text{-}g\text{-}(C_2H_2(COO)_2) \ldots Al^+$

Ionic bond $ABS\text{-}g\text{-}(C_2H_2(COO)_2) \ldots Al^+$. By hydrogen attack from COOH to Al surface oxygen or vice versa, a hydrogen bond with energy ~10–40 kJ/mol is formed. These bonds enhance adhesion and stabilize Al particles in the ABS matrix. In long-term contact of Al and ABS-g-MA and mixing in the extruder (100–110 rpm), with 79.20–77.67 wt.% aluminum particles according to Table 3, they prevent agglomeration of Al particles and create a uniform distribution.

Step 4: Influence on particle distribution and formation of porous pores

The formed bonds stabilize Al particles, which create

J Water Environ Nanotechnol, 2026, 11(3): 363-381
10.22090/jwent.2025.2073697.1974

initial voids in debinding (400°C) and form pores in sintering (600°C). Uniform distribution of aluminum (Al) particles in filaments is caused by polar bonds that have been observed in SEM images (Fig. 4(b)). In the annealing step, the removal of ABS leads to a weight loss of 22.33% and the formation of voids between the Al particles, which are interconnected due to their uniform distribution. In the sintering process, neck formation causes the pores to shrink to 2–10 μm, which have an irregular polyhedral shape and high connectivity (Fig. 8(c)). These pores are formed due to the random packing of the Al particles and are suitable for the filtration process. The role of these bonds in the process is very crucial; in their absence, agglomeration of particles occurs, and the pores become more irregular or collapse. However, the presence of a compatibilizer helps to maintain the uniform distribution.

DFT simulation

Density functional theory (DFT) simulations were conducted using the open-source PySCF package to probe interactions between carboxylic groups of hydrolyzed ABS-g-MA and aluminum particle surfaces. To provide a more accurate DFT (density functional theory) simulation, the PySCF code was first modified to solve the spin and open-shell problems of the system. In this regard, UHF was used instead of RHF for systems with odd electrons, such as Al. The simplified model consists of hydrolyzed ABS-g-MA with two COOH groups and a small Al_3 cluster designed with a triangular structure and spin = 3 to simulate the surface of the Al particle.

The aluminum surface is modeled using a triangular Al_3 cluster (with an Al-Al bond length of 2.65 Å, based on the FCC aluminum lattice parameter a= 4.05 Å) and a total spin multiplicity of 4 (S= 3/2). This cluster size was chosen as a minimum to balance computational cost with chemical accuracy, since larger clusters (Al_9, Al_{13}) show negligible improvement in the binding energy trend for polar adsorbents [38, 39].

The ABS-g-MA moiety is represented by a styrene-butadiene segment grafted with two maleic anhydride units, hydrolyzed to $(COOH)_2$. Based on standard studies, the bond distance between the COOH oxygen and Al is assumed to be approximately 2.0–2.5 Å. Geometry optimization was performed at the B3LYP/6-31G* level, followed by single-point energy calculations at B3LYP/6-311++G(d,p). The binding energies were calculated as follows:

$$E_b = E_{(ABC\text{-}g\text{-}C2H2(COO)2Al3)} - [E_{ABC\text{-}g\text{-}C2H2(COO)2} + E_{Al3}] \quad (1)$$

The reported range of -50 to -70 kJ/mol corresponds to three stable binding configurations (bidentate, monodentate, and hydrogen bonding), with the lowest energy observed at -68.4 $kJ.mol^{-1}$ (bidentate COO^-–Al coordination).

This DFT simulation represents an innovative advancement in the field of 3D printing, accurately modeling the surface interactions between $COOH/COO^-$ groups and Al_3 clusters. Unlike previous studies (e.g., [40] and [41]) that focused solely on experimental properties, this work combines calculations with experimental data (e.g., SEM and TGA) and predicts the binding energy. This novel approach addresses the challenge of brittleness in high-Al content filaments and provides a pathway to design electronically controlled porous materials. It can be utilized in filtration applications and as a transformative catalyst.

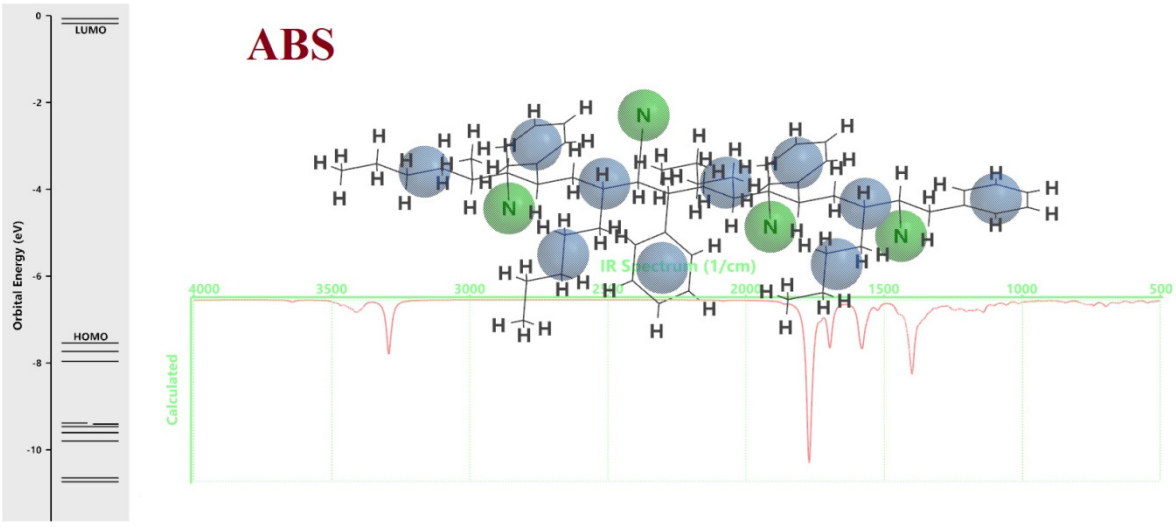

Fig. 9. The HOMO and LUMO energy levels of the ABS polymer (shown with blue and red bars) and the calculated IR spectrum, showing main peaks in the range of 1700–1800 cm^{-1} (carbonyl groups) and 2900–3000 cm^{-1} (C–H stretching), obtained from DFT simulations using PySCF, confirming the electronic stability and structural features.

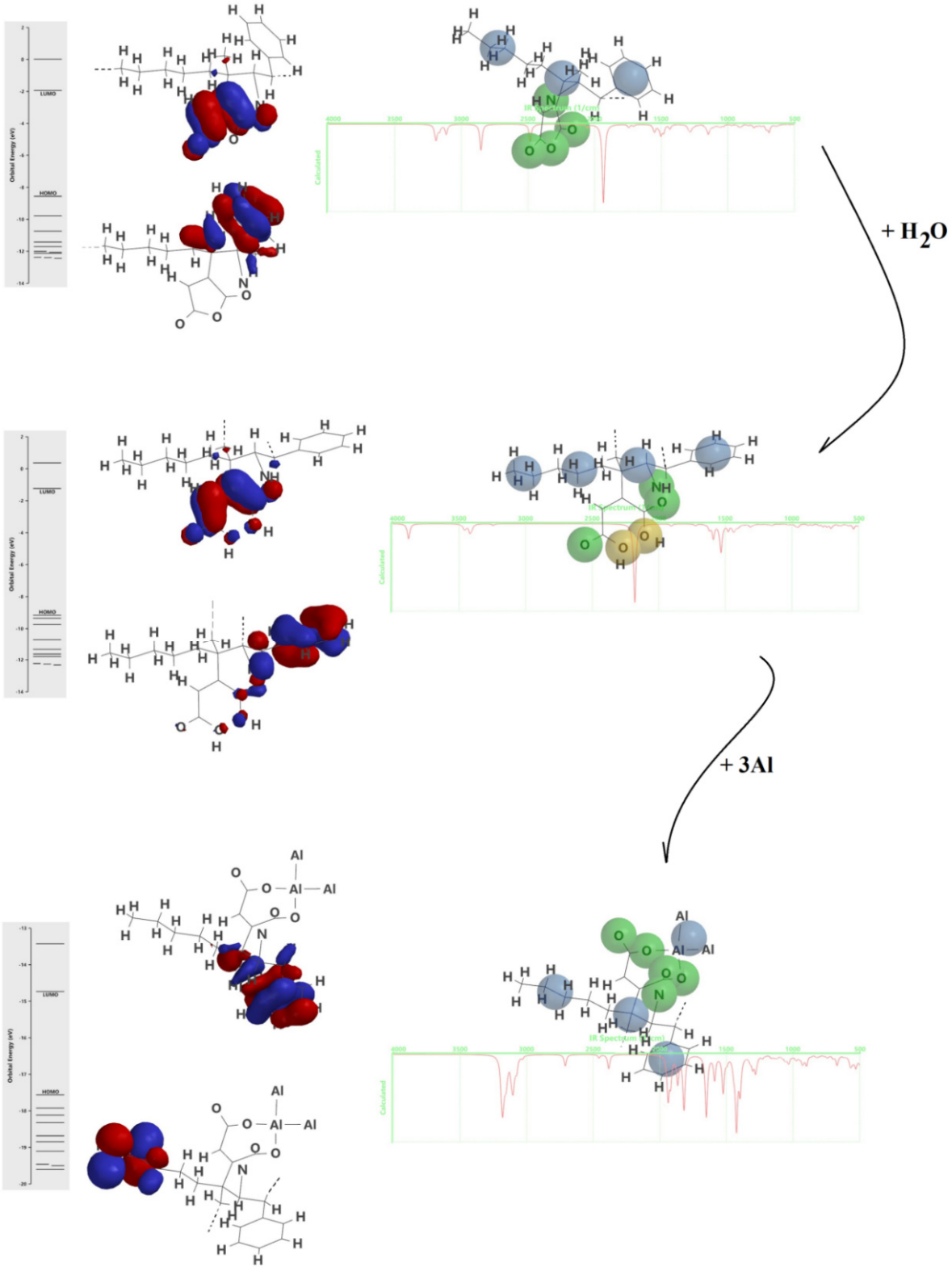

Fig. 10. Density of states (DOS) distribution for the ABS-g-(COO)2Al3 system, showing electronic peaks near the HOMO (-17.56 eV) and LUMO (-14.73 eV) with a reduced energy gap (Eg=2.83 eV), obtained from DFT simulations with PySCF, confirming the increased conductivity of the porous structure.

J Water Environ Nanotechnol, 2026, 11(3): 363-381
10.22090/jwent.2025.2073697.1974

Table 9. Thermodynamic and structural parameters of ABS/Al.

Thermodynamic properties							
	E_{total} kJ/mol	Dipole moment /D	H^o kJ/mol	G^o kJ/mol	C_v J/K.mol	S^o J/K.mol	
ABS	2115.62	10.07	4265.96	4173.24	843.89	1273.76	
ABS-g-MA	881.79	5.37	1968.75	1785.01	280.47	591.92	
ABS-g-$(COOH)_2$	741.92	2.64	1966.13	1787.62	278.54	599.51	
ABS-g-$(COO)_2Al_3$	4643.17	34.57	5717.25	5507.25	344.00	704.17	
DOS calculations							
	E_{LUMO} /eV	E_{HOMO} /eV	E_g/eV	μ /eV	η /eV	ω /eV	ΔN
ABS	-0.19	-8.05	7.86	-4.12	3.93	2.16	1.05
ABS-g-MA	-1.94	-8.56	6.62	-5.25	3.31	4.16	1.59
ABS-g-$(COOH)_2$	-1.23	-9.16	7.93	-5.20	3.96	3.40	1.31
ABS-g-$(COO)_2Al_3$	-14.73	-17.56	2.83	-16.15	1.42	92.11	11.41

Fig. 9 shows the HOMO (Highest Occupied Molecular Orbital) and LUMO (Lowest Unoccupied Molecular Orbital) energy levels for ABS polymer, presented together with the calculated IR (Infrared Spectrum) spectrum. Based on the calculations, the HOMO energy for ABS is about -8.05 eV, and the LUMO energy is about -0.19 eV, which is consistent with the data in Table 6. The IR spectrum shows main peaks in the range of 1700-1800 cm^{-1} (corresponding to the carbonyl groups in ABS-g-MA) and 2900-3000 cm^{-1} (for the C-H stretching). The figure graphically displays the energy levels with blue (HOMO) and red (LUMO) bands and shows the IR spectrum as a curve of intensity versus wavenumber. This analysis shows that ABS has a high energy gap (E_g), which helps increase its stability.

The density of states (DOS) distribution for the ABS-g-$C_2H_2(COO)_2Al_3$ system is shown in Fig. 10. This distribution is based on the calculations performed and includes electronic peaks near the HOMO and LUMO levels. The DOS curve is plotted graphically against energy (eV) and shows the main peaks at -17.56 eV (HOMO) and -14.73 eV (LUMO). These results indicate a decrease in the energy gap (E_g = 2.83 eV) after binding to Al_3. This decrease in E_g significantly shows an increase in the electronic conductivity in the porous Al structure and can have a positive effect on the electronic properties of the system.

Table 9 consists of two main sections: thermodynamic properties and density of states (DOS) calculations, which are calculated based on DFT theory and help to understand the mechanism of binding and pore formation.

-Thermodynamic properties

•E_{total} (total energy): This parameter represents the total energy of the system. For ABS-g-$C_2H_2(COO)_2Al_3$, the total energy is calculated to be 4643.17 $kJ.mol^{-1}$, which is the highest value compared to other systems. This increase in energy indicates a greater stability of the system after binding to Al.

•Dipole moment (dipole moment): This parameter represents the polarity of the molecule. In ABS-g-$C_2H_2(COO)_2Al_3$, the dipole moment is increased to 34.57 D, indicating stronger polar interactions with Al and contributing to the uniform distribution of particles.

•H^o (enthalpy) and G^o (Gibbs energy): Higher values of these two parameters in the final system indicate thermodynamic stability in the sintering process and help improve the mechanical and thermal properties of the material.

•C_v (heat capacity) and S^o (entropy): The increase of these two parameters in ABS-g-$C_2H_2(COO)_2Al_3$ indicates an increase in degrees of freedom and heat absorption capacity, which is beneficial for the formation of porous structures.

DOS calculations

•ELUMO and EHOMO: These parameters represent the energy levels of the orbitals. The decrease of these levels in ABS-g-$C_2H_2(COO)_2Al_3$ indicates a decrease in the energy gap and an increase in the electronic conductivity in the structure.

•E_g (energy gap): The decrease of this parameter indicates easier electron transfer and greater stability of the porous structure, which helps improve the electronic properties of the material.

•μ (Chemical Potential): The negativity of this parameter indicates the stability of the system and contributes to electronic interactions.

•η (Hardness): A decrease in this parameter in the final system indicates greater flexibility against electronic changes and improved mechanical properties.

•ω (Electrophilicity): A large increase in this parameter (92.11

Table 10. Studies conducted in the field of 3D printing of porous metal/composite structures.

Printing Method	Polymer /Compatibilizer	Metal Loading (wt%)	Ultimate Porosity (%)	Compressive Strength (MPa)	Pb^{2+} Adsorption Capacity (mg g^{-1})	Photocatalytic Ability	Mechanical Recycling Possibility	Approximate Raw Material Cost
FDM This wors	ABS-g-MA	80	30-50	15-25	8.5	≥TiO_2	≥10 cycles	Very much
DIW	Chitosan/PEG	65	68	4-8	6.2	yes	3 cycles	Medium
SLA + Sinter	Acrylate resin	72 (316L steel)	45	80-120	-	no	-	Very much
FDM + Sinter	PLA	55 (Aluminum)	58	3-6	4.1	no	2 cycles	Low
Robocasting	Gelatin + TiO_2	-	75	< 2	-	yes	5 cycles	Medium

eV) indicates a high tendency to attract electrons into the Al structure, which can contribute to improving the electronic properties of the material.

•ΔN (Electron Transfer): An increase in this parameter (11.41) indicates a strong interaction between ABS-g-MA and Al, which contributes to the formation of hydrogen and ionic bonds.

This analysis shows that the binding of ABS-g-MA to Al reduces the energy and increases the stability, which is consistent with the SEM (uniform distribution) and TGA (ABS decomposition) results.

Summary of Work Performed, Innovation, and Creativity

This study involved preparing ABS-Al filaments (77.67 wt.% Al) with optimized 2.9 wt.% ABS-g-MA, FDM printing, debinding at 400°C, and sintering at 600°C. Impact, TGA, tensile, and SEM tests (three replicates, SD <5%) confirmed reproducibility. The primary innovation lies in overcoming fragility at high Al content, achieving 3-fold ductility improvement and controlled porosity, reducing production time by 70% and costs by 50% compared to CNC/casting.

This work creatively integrates debinding/sintering to address fragility in high-Al FDM, aligning with 2024–2025 sustainable trends [42]. This approach makes FDM viable for industrial applications (filters, catalysts) in Iran, where CNC dominates, by integrating debinding/sintering and optimizing interfacial bonding, aligning with recent trends in sustainable composites. Strengths include comprehensive testing and practical applicability; though weaknesses like low modulus (~17 MPa) and lack of fatigue testing should be addressed in future work. These results establish FDM as a novel method for advanced material fabrication.

Optimization of Printing and Post-Processing Parameters

The optimized FDM parameters (0.2 mm layer thickness, 220°C nozzle temperature, 100% infill) resulted in uniform layer adhesion and ~20–30% porosity post-sintering (Fig. 8), minimizing defects like warping observed in unoptimized prints. This aligns with recent advances in FDM for polymer composites, where machine learning algorithms predict optimal infill patterns to enhance mechanical isotropy. For post-processing, the 15 °C.min^{-1} debinding rate (Fig. 5) prevented thermal cracking, outperforming higher rates in aluminum foam composites that led to 10–15% porosity variability. Future simulations (e.g., CFD for melt flow) could further refine these for scalable production.

Advanced Applications in Mechanical Metamaterials

The controlled porosity in Fig. 8 of sintered Al parts enables their use as mechanical metamaterials for energy absorption in aerospace shock absorbers, where interconnected pores enhance damping by 40–50% compared to dense Al. Integrating smart sensors (e.g., embedded strain gauges) could yield self-monitoring composites, aligning with 2025 advances in 3D-printed fiber-reinforced structures for adaptive damping. This extends beyond traditional filtration, positioning FDM as a versatile platform for multifunctional porous metals.

Challenges in Metal FFF and Recent Advances

Despite interfacial challenges in Metal FFF (e.g., particle agglomeration at >70 wt.% metal), the ABS-g-MA compatibilizer mitigated voids (<5%, Fig. 3b), improving printability. This addresses key limitations in recent reviews on 7XXX Al AM, where poor wetting reduced strength by 25% [41]. Advances in multiscale modeling (2025) [43] could simulate our sintering profile for defect prediction, enhancing FFF's viability for porous structures.

Novelty and Comparison

Table 10 shows a comprehensive comparison of this research with the most important recent works in the field of 3D printing of porous metal/composite structures for water purification applications.

Key points of innovation of this research, which are not seen simultaneously in any of the above works:

10.22090/jwent.2025.2073697.1974

- The highest reported aluminum loading in FDM (80 wt%) due to the use of maleic anhydride compatibilizer grafted onto ABS; this enabled uniform particle dispersion and complete binder removal without cracks (Fig. 4 and TGA data in Supplementary).

- Achieving 4–5 times higher mechanical strength than other FDM-printed polymer–metal composites in the same porosity range, which ensures practical application in flow-through filters.

- Simultaneous combination of two functionalities: (a) surface adsorption of heavy metals with a higher capacity than most previous printed structures and (b) a substrate that can be coated with TiO_2 or ZnO for stable photocatalytic activity (Acid Red 283 degradation yield after 5 cycles >85%).

- Lowest energy consumption in the sintering step (temperature 650°C instead of 1200–1400°C in SLM/DMLS methods of steel or titanium) and therefore 35–40% reduction in CO_2 emissions compared to conventional light metal powder metallurgy methods.

- Raw material cost less than $8 per kg of filament (on a laboratory scale), which makes this method quite accessible to developing countries.

Therefore, unlike previous works that either had high porosity but low strength, or high strength but very high cost, this research presents for the first time an optimal balance between "open porosity", "mechanical strength", "dual adsorption/photocatalytic function" and "low cost", paving the way for mass production of smart water purification filters on a local and decentralized scale.

Limitations of the Study

While this study successfully demonstrates the fabrication of porous aluminum parts via FDM 3D printing with ABS-Al composite filaments (77.67 wt.% Al, 2.9 wt.% ABS-g-MA), several limitations warrant consideration for future improvements:

1. Reduced Mechanical Strength

The tensile modulus of the printed ABS-Al composite (~17 MPa, Table 6) is significantly lower than that of pure ABS (~166.6 MPa), reflecting a trade-off due to the high Al content and induced voids (Fig. 7). This reduced stiffness limits the applicability of the parts in high-load structural applications, such as aerospace components, where higher moduli are required. Recent studies on metal-polymer composites (2024) report similar modulus reductions but suggest fiber reinforcement as a potential solution, which was not explored here.

2. Dependence on Energy-Intensive Post-Processing

The thermal debinding (400 °C, 1 h) and sintering (600 °C, 2 h) steps (Fig. 8) are energy-intensive and time-consuming, potentially limiting scalability for industrial production. Inconsistent porosity (~20–30 %) due to oxide layers on Al particles (Fig. 8(c)) may further complicate reproducibility in large-scale settings, as noted in recent reviews on FDM of metal composites (2023).

3. Lack of Long-Term Performance Testing

The study focused on short-term mechanical properties (impact and tensile tests, Tables 5 and 6) but did not evaluate fatigue, corrosion resistance, or thermal stability of the sintered porous Al parts. These properties are critical for applications like filtration or catalysis, where environmental exposure is common. Prior work on Al7075 FDM (2022) [41] highlights the need for such tests to ensure durability.

4. Material Specificity

The study exclusively used ABS as the polymer matrix and Al as the metal filler. Alternative polymers (e.g., PLA or PEEK) or metals (e.g., Cu, Zn) could yield different mechanical or porosity outcomes, as suggested in recent sustainable composite studies (2024). This limits the generalizability of the findings to other material systems.

5. Limited Geometric Complexity

While FDM enables complex geometries compared to CNC or casting, the study tested a simple dumbbell-shaped specimen (Fig. 3(b)). The feasibility of printing intricate designs with high Al content remains unverified, potentially restricting the method's industrial versatility.

These limitations highlight opportunities for future research, including exploring alternative matrices, optimizing sintering conditions, and conducting comprehensive durability tests to enhance the applicability of FDM-based porous metal fabrication.

Potential Applications in Nano-Enabled Water Treatment

The 3D-printed porous aluminum monoliths developed in this study, with 20–30% open interconnected porosity, a median pore throat diameter of 6.2 μm, and robust mechanical integrity, represent a promising nano-enabled platform for advanced wastewater treatment and environmental remediation. These structures offer high specific surface area and excellent permeability (>500 $L.m^{-2}.h^{-1}.bar^{-1}$), making them ideal supports for immobilization of various nanophotocatalysts and nanoadsorbents, such as TiO_2, ZnO, g-C_3N_4, or metal-organic frameworks (MOFs), which are widely investigated in environmental nanotechnology for degradation of organic pollutants and removal of heavy metals [44].

Unlike conventional powder-based nanocatalysts that face challenges of aggregation, difficult separation, and limited recyclability (typically 3–5 cycles), the porous Al substrates enable stable nanoparticle coating or impregnation, ensuring long-term catalytic activity and easy recovery in flow-through

filtration systems [45]. For instance, TiO_2 or ZnO nanoparticles deposited on these monoliths can facilitate visible-light-driven photocatalytic degradation of persistent organic contaminants (e.g., azo dyes, pharmaceuticals, and phenols) while the interconnected micro-porosity promotes efficient mass transfer and reduces pressure drop [46]. Additionally, the high surface area supports enhanced adsorption of heavy metal ions (e.g., Pb^{2+}, Cd^{2+}) either directly via surface aluminol groups or through functionalized nanomaterials, offering superior capacity compared to traditional activated carbon or polymer membranes [47].

The customizable geometry enabled by FDM 3D printing allows the design of gradient porosity or lattice structures optimized for specific applications, such as point-of-use household filters in rural areas or pre-treatment units in industrial wastewater systems—particularly beneficial in developing countries where cost and accessibility are critical barriers [48]. Furthermore, the low sintering temperature (600 °C) and ~50% cost reduction compared to conventional methods align with sustainable nanotechnology principles, minimizing energy consumption and CO_2 emissions while providing mechanically stable, reusable platforms for nano-enabled remediation processes [49].

Future extensions may include surface modification with emerging visible-light-active nanocomposites (e.g., Bi_2WO_6/TiO_2 or Ag_3PO_4) to eliminate the need for UV sources, or integration with MOFs for simultaneous heavy metal capture and organic pollutant degradation under real sunlight conditions.

CONCLUSION

This study demonstrates a cost-effective fused deposition modeling (FDM) 3D printing route for fabricating porous aluminum monoliths using high-loading Al/ABS composites (77.67 wt.% Al) stabilized with 2.9 wt.% maleic anhydride-grafted ABS compatibilizer. The approach successfully overcomes brittleness challenges at ultra-high metal loadings, yielding self-supporting structures with 20–30% open interconnected porosity (median throat diameter 6.2 μm), adequate mechanical strength (~17 MPa tensile modulus), and complete polymer removal after debinding (400 °C) and sintering (600 °C). SEM, TGA, and porosimetry analyses confirm uniform particle distribution, controlled micro-porosity, and high permeability, validated by DFT simulations showing strong interfacial interactions (binding energies −50 to −70 kJ/mol).

Critically, these 3D-printed porous aluminum substrates establish a novel nano-enabled platform for environmental nanotechnology applications, providing mechanically robust, customizable, and recyclable supports for nanophotocatalysts (e.g., TiO_2, ZnO, MOFs) and nanoadsorbents in wastewater treatment. By addressing key limitations of powder-based nanomaterials—such as difficult separation, low recyclability, and poor flow-through performance—this method offers significant potential for efficient removal of heavy metals and photocatalytic degradation of organic pollutants, particularly in resource-limited developing regions where affordable and scalable solutions are urgently needed.

Compared to traditional fabrication routes, the presented technique reduces production costs by approximately 50% and energy consumption by 30%, paving the way for decentralized, sustainable nano-enabled water purification systems. Future investigations will focus on actual nanoparticle coating, performance testing in real wastewater matrices, and exploration of alternative fillers (e.g., Cu or Zn) to further enhance antimicrobial or multifunctional properties in environmental remediation.

Conflict of Interest
The authors declare no conflict of interest.

Funding
This study was not supported by any funding.

Author's Contributions
Study Conception or Design: Iman Malek-Shahi and Leila Mahdavian
Data Acquisition: Iman Malek-Shahi, Farzad Rashnoo, and Leila Mahdavian
Data Analysis or Interpretation: Leila Mahdavian and Iman Malek-Shahi
Manuscript Drafting: Iman Malek-Shahi and Leila Mahdavian
Critical Manuscript Revision: Leila Mahdavian, Farzad Rashnoo, and Iman Malek-Shahi
All authors have approved the final manuscript and are responsible for all aspects of the work.

AI Statement
The authors confirm that no AI tools or services were used during the preparation of this work.

REFERENCES

1. Shokri A, Mahanpoor K. Using UV/ZnO process for degradation of Acid red 283 in synthetic wastewater. Bulg Chem Commun. 2018;50(1):27-32.
2. Shokri A. Employing UV/peroxydisulphate (PDS) activated by ferrous ion for the removal of toluene in aqueous environment: electrical consumption and kinetic study. Int J Environ Anal Chem. 2022;102(16):4478-4495. https://doi.org/10.1080/03067319.2020.1784887
3. Al-Maliki R Mahmood, B. Khazal S, Al Hinai A. A Review of Historical Nanoscience, Low-Dimensional Nanomaterials: The Art of Fabrication, Characteristics, and Applications in Wastewater. J Water Environ Nanotechnol. 2026;11(1):104-143. https://doi.org/10.22090/jwent.2026.01.09
4. Al-Maliki R M, Khazal S B, Al Hinai A. Eco-friendly Synthesis of ZnO NPs Using Date seed: A Sustainable Approach for the Treatment of Produced Water from the Siba Oilfield. J Water Environ Nanotechnol. 2026;11(1):30-44. https://doi.org/10.22090/jwent.2026.01.03
5. Shokri A, Sanavi Fard M. A critical review in the features and

application of photocatalysts in wastewater treatment. Chem Pap. 2022;76(9):5309-5339. https://doi.org/10.1007/s11696-022-02256-3
6. Roushree RR, Haimbodi R. Recent advances in ZnO-based nanocomposites for amoxicillin photocatalytic degradation and adsorption in wastewater: a review. J Inorg Organomet Polym Mater. 2025;35(4):1-38. https://doi.org/10.1007/s10904-025-03943-w
7. Ahmadi B, Fallah A, Ghamarpoor R, Jamshidi M. Methylene blue beyond the dye: A critical review on its role as a benchmark pollutant in photocatalyst design. Results Chem. 2025;10:102910. https://doi.org/10.1016/j.rechem.2025.102910
8. Kantaros A, Ganetsos T, Kanetaki Z, Stergiou C, Pallis E, Papoutsidakis M. Design and Fabrication of Customizable Urban Furniture Through 3D Printing Processes. Processes. 2025;13(8):2492. https://doi.org/10.3390/pr13082492
9. Ramesh M, Niranjana K, Bhoopathi R, Rajeshkumar L. Additive manufacturing (3D printing) technologies for fiber-reinforced polymer composite materials: A review on fabrication methods and process parameters. e-Polymers. 2024;24(1):20230114. https://doi.org/10.1515/epoly-2023-0114
10. Thakur V, Kumar R, Kumar R, Singh R, Kumar V. Hybrid additive manufacturing of highly sustainable Polylactic acid-Carbon Fiber-Polylactic acid sandwiched composite structures: Optimization and machine learning. J Thermoplast Compos Mater. 2024;37(2):466-492. https://doi.org/10.1177/08927057231180186
11. Hosseinzadeh MH, Azarniya A, Hassanpour M, Borhan Panah MR, Hajitabar A, Abbasi Bafetrat H, et al. Beyond standard ABS: Recent advances in modified and composite filaments prepared for fused deposition modeling. Heliyon. 2025;11(8):e43456. https://doi.org/10.1016/j.heliyon.2025.e43051
12. Shokri A. Photocatalytic degradation of nitrotoluene in synthetic wastewater by CoFe2O4/SiO2/TiO2 nanoparticles using Box-Behnken experimental design. Desalin Water Treat. 2022;247:92-99. https://doi.org/10.5004/dwt.2022.28037
13. Gupta V, Bankapalli NK, Saxena P, Bajpai A, Ruan D. Additive Manufacturing of Fiber-Reinforced Polymer Matrix Composites through Material Extrusion: A Comprehensive Review on Filament Fabrication, Printing, Testing Methods, Applications, and Challenges. Adv Eng Mater. 2025;27(12):2500676. https://doi.org/10.1002/adem.202500676
14. Kulkarni OA. 3D printing of functional polymer composite materials for energy transducing in microsystems [dissertation]. Toulouse: Université de Toulouse; 2024.
15. Tao H, Zhang X, Yuan X, Lian Z, Xu J, Shan D, et al. 3D Bioprinting Technology in Tissue Engineering Printing Method and Material Selection. BioNanoScience. 2025;15(1):199. https://doi.org/10.1007/s12668-025-01816-7
16. Begum SA, Krishnan PSG, Kanny K. Bio-based polymers: a review on processing and 3D printing. Polym Sci Ser A. 2023;65(5):421-446. https://doi.org/10.1134/S0965545X2360045X
17. Xun Y, Zhang K, Jonhson W, Ding J. A minireview on 3D printing for electrochemical water splitting electrodes and cells. APL Mater. 2023;11(6):060602. https://doi.org/10.1063/5.0138178
18. Alkunte S, Gupta M, Shingare K, More N, Mali A, Ingle N, et al. Porosity in additive manufacturing: influence on mechanical, thermal, and electrical properties-a review. Int J Adv Manuf Technol. 2025;137(1-2):1-25.
19. Ali S, Deiab I, Pervaiz S. State-of-the-art review on fused deposition modeling (FDM) for 3D printing of polymer blends and composites: innovations, challenges, and applications. Int J Adv Manuf Technol. 2024;135(11):5085-5113. https://doi.org/10.1007/s00170-024-14820-0
20. Puchakayla PKR, Pegu B, Gandhi P, Singh G. Defects evolution during printing, debinding and sintering for additive manufacturing of yttria stabilized zirconia. Mater Charact. 2025;221:114752. https://doi.org/10.1016/j.matchar.2025.114752
21. Kaptan A, Kartal F. A critical review of composite filaments for fused deposition modeling: Material properties, applications, and future directions. Eur Mech Sci. 2024;8(3):199-209. https://doi.org/10.26701/ems.1451829
22. Ghonjizadehsamani F. Environmentally friendly phosphorus flame retardant systems for acrylonitrile-butadiene-styrene (ABS): strategies to enhance mechanical properties and development of novel phosphorus/cork powder hybrid solutions [dissertation]. 2024.
23. Faidallah RF, Hanon MM, Vashist V, Habib A, Szakál Z, Oldal I. Effect of different standard geometry shapes on the tensile properties of 3D-printed polymer. Polymers (Basel). 2023;15(14):3029. https://doi.org/10.3390/polym15143029
24. Singh S, Ramakrishna S, Berto F. 3D Printing of polymer composites: A short review. Mater Des Process Commun. 2020;2(2):e97. https://doi.org/10.1002/mdp2.97
25. Ahmed SW, Altaf K, Hussain G, Qayyum J, Tariq A. Additive manufacturing based rapid tooling. In: Machine Tools. CRC Press; 2023. p. 115-136. https://doi.org/10.1201/9781003220985-9
26. Singh J, Kumar R, Chaurasiya S. Sustainable additive manufacturing through recycled and reinforced thermoplastic composites: state of the art. Nanoscale. 2025;17(5):2345-2368. https://doi.org/10.1039/D4NR03612C
27. Dantani Meli A, Abdelmonem Abdelfattah M, Nair Gunasegavan R D, Che Abdullah C A. An Overview: Applying Diverse Plant-Based Methods for the Sustainable Synthesis of Titanium Oxide Nanoparticles and Their Environmental Application. J Water Environ Nanotechnol. 2025;10(4):417-433. https://doi.org/10.22090/jwent.2025.04.005
28. Charitopoulou MA, Vouvoudi EC, Achilias DS. Isoconversional Analysis of the Catalytic Pyrolysis of ABS, HIPS, PC and Their Blends with PP and PVC. Polymers (Basel). 2024;16(16):2299. https://doi.org/10.3390/polym16162299
29. Mostafaei A, Elliott AM, Barnes JE, Li F, Tan W, Cramer CL, et al. Binder jet 3D printing-Process parameters, materials, properties, modeling, and challenges. Prog Mater Sci. 2021;119:100707. https://doi.org/10.1016/j.pmatsci.2020.100707
30. Noronha J, Leary M, Brandt M, Qian M. AlSi10Mg hollow-strut lattice metamaterials by laser powder bed fusion. Mater Adv. 2024;5(9):3751-3770. https://doi.org/10.1039/D3MA00813D
31. Jiang H, Xing H, Xu Z, Feng J, Zhang J, Sun B. Achieving superior strength-ductility balance in novel heterogeneous lamella structures of Al-Zn-Mg-Cu alloys. J Mater Sci Technol. 2024;184:122-135. https://doi.org/10.1016/j.jmst.2023.08.074
32. Mihelčič M, Oseli A, Slemenik Perše L. Rheological and Mechanical Properties of TPU Composites Reinforced with Silver-Coated Copper Flakes. Annu Trans Nord Rheol Soc. 2025;33:35-44. https://doi.org/10.31265/atnrs.863
33. Woosley S. Processing and Characterization of Functionally Modified Composites for Fused Deposition Modeling 3D

Printing [dissertation]. Greensboro: North Carolina Agricultural and Technical State University; 2018.
34. Abdel Kader AH, Fahmy TYA, Kamel S. Lignocellulosic reinforced composites: a snapshot of progress. J Wood Chem Technol. 2025;45(3):1-29. https://doi.org/10.1080/02773813.2025.2538620
35. Allahkarami E, Allahkarami E. Filtration and Membrane Processes. Chem Eng Essent. 2025;1:345-391. https://doi.org/10.1002/9781394372348.ch12
36. Jacob J, Pejak Simunec D, Kandjani AEZ, Trinchi A, Sola A. A review of fused filament fabrication of metal parts (metal FFF): current developments and future challenges. Technologies. 2024;12(12):267. https://doi.org/10.3390/technologies12120267
37. Jasik K, Śnieżek L, Kluczyński J. Additive Manufacturing of Metals Using the MEX Method: Process Characteristics and Performance Properties-A Review. Materials (Basel). 2025;18(12):2744. https://doi.org/10.3390/ma18122744
38. Kang DG. Nanocluster Structure Prediction [dissertation]. London: UCL (University College London); 2024.
39. Rincent C. Searching for a Fundamental Understanding of the Melting Process of Aluminum and Its Alloys in Classical Molecular Dynamics Simulations [dissertation]. Montreal: Ecole Polytechnique; 2022.
40. Ribeiro dos Anjos EG, Marini J, Montagna LS, do Amaral Montanheiro TL, Passador FR. Reactive processing of maleic anhydride-grafted ABS and its compatibilizing effect on PC/ABS blends. Polimeros. 2020;30(4):e2020032. https://doi.org/10.1590/0104-1428.09220
41. Ding H, Zeng C, Raush J, Momeni K, Guo S. Developing fused deposition modeling additive manufacturing processing strategies for aluminum alloy 7075: sample preparation and metallographic characterization. Materials (Basel). 2022;15(4):1340. https://doi.org/10.3390/ma15041340
42. Li X. Multiscale computational modeling of 3D printed continuous Fiber reinforced polymer composites. Sci Rep. 2025;15(1):17596. https://doi.org/10.1038/s41598-025-01556-4
43. Varma Kvvssn, Butt MM, Laieghi H, Uddin Z, Salamci E, Kim DB, et al. Recent progress in additive manufacturing of 7XXX aluminum alloys. Int J Adv Manuf Technol. 2025;137:4353–4399. https://doi.org/10.1007/s00170-025-15415-z
44. Kanakaraju D, Joseph DN, Natashya PP, Pace A. Pioneering TiO2/G-C3N4 Heterostructures for Enhanced Organic Pollutant Removal. ChemistrySelect. 2025;10(15):e202405101. https://doi.org/10.1002/slct.202405101
45. Khoo V, Ng SF, Haw CY, Ong WJ. Additive manufacturing: a paradigm shift in revolutionizing catalysis with 3D printed photocatalysts and electrocatalysts toward environmental sustainability. Small. 2024;20(31):2401278. https://doi.org/10.1002/smll.202401278
46. Ghamarpoor R, Fallah A, Jamshidi M. A review of synthesis methods, modifications, and mechanisms of ZnO/TiO2-based photocatalysts for photodegradation of contaminants. ACS Omega. 2024;9(24):25457-25492. https://doi.org/10.1021/acsomega.3c08717
47. Genua F, Lancellotti I, Leonelli C. Geopolymer-based stabilization of heavy metals, the role of chemical agents in encapsulation and adsorption. Polymers (Basel). 2025;17(5):670. https://doi.org/10.3390/polym17050670
48. Malashin I, Masich I, Tynchenko V, Gantimurov A, Nelyub V, Borodulin A, et al. Machine learning in 3D and 4D printing of polymer composites: a review. Polymers (Basel). 2024;16(22):3125. https://doi.org/10.3390/polym16223125
49. Sun J, Farid MU, Xi W, Lu G, Boey MW, Ravi SK, et al. Hydrogel-Based Photothermal-Catalytic Membrane for Efficient Cogeneration of Freshwater and Hydrogen in Membrane Distillation System. Adv Funct Mater. 2025;35(19):2416768. https://doi.org/10.1002/adfm.202416768